PIC/fluid/wave Simulation of the Plasma Discharge in an ECR Plasma Thruster

IEPC-2019-633

Presented at the 36th International Electric Propulsion Conference
University of Vienna, Austria
September 15-20, 2019

A. Sánchez-Villar[*], J. Zhou [†], Mario Merino[‡], Eduardo Ahedo[§]
Equipo de Propulsión Espacial y Plasmas (EP2), Universidad Carlos III de Madrid, Leganés, Spain

We present the first self-consistent, complete simulations of the Big-Magnet electron-cyclotron resonance thruster (ECRT) developed by ONERA. The simulation uses a hybrid PIC/fluid model for the plasma transport and a frequency-domain full-wave model for the electromagnetic fields based on an adaptable mesh and a collisional cold plasma dielectric description. Plasma properties and electromagnetic fields are shown for the nominal operating point. Most of the electromagnetic power absorption is due to radial electric fields near the ECR region. The simulation shows that the ECRT plasma discharge contains multiple electromagnetic wave propagation regimes, and the sensitivity of the wavefields on the the plasma profiles.

I. Introduction

The electron cyclotron resonance thruster (ECRT[1–7]) is an electric propulsion concept that relies on the localized absorption of electromagnetic power at region the electron-cyclotron resonance (ECR), and a magnetic nozzle (MN) to generate thrust. The use of radio-frequency (RF) heating allows to eliminate electrodes and simplify the power processing unit of the device.

The first publication of this propulsion concept was made in 1962.[8] In Ref.2, a 2% efficiency thruster with 22% energy and 80-90% coupling efficiencies were reported for a 320W argon prototype without performing any optimization investigation of the device. In Refs.3, 4 devices up to 15% thrust efficiency were built and test. Then, in the 1990's, a comparison between experimental and theoretical research[5,7,9] reported a large difference between the expected and measured jet and coupling efficiencies of an argon tested device (e.g. 2% compared to a 41% net jet efficiency or a 30% coupling efficiency compared to a 98%). For instance, the high coupling efficiencies had been reported by other works.[2,10] This disagreement was explained in multiple occasions due to the inadequate diagnostics setup and equipment, specially to measure coupling losses as well as the lack of a complete model. Thus, the literature proved the need of future experimental and theoretical campaigns that improved the existing diagnostics and models of this type of discharges. Currently, only an ECR heated version of the ion thruster has operated in a space mission.[11]

Recently, a gridless ECR plasma thruster concept was recognized as a disruptive electric propulsion technology by the European actors and the MINOTOR[12] project H2020 was funded to mature such technology up to a TRL 4-5, demonstrating its feasibility. The concept uses a novel design[13] with a coaxial line used to feed electromagnetic power in the order of tenths of watt with a smaller thruster than in previous works. In the context of MINOTOR, ONERA is the leading actor in the development of the coaxial prototype and the associated experimental setup.

In the context of the same project, EP2 group from Universidad Carlos III de Madrid (UC3M) has developed SURFET (SimUlator for RF Electrodeless Thrusters). The main goal of this code is to provide

---

[*] PhD student, Aerospace Engineering department, alvaro.sanchez.villar@uc3m.es.

[†] PhD student, Bioengineering and Aerospace Engineering department,

[‡] Assistant Professor, Aerospace Engineering department, mario.merino@uc3m.es.

[§] Professor, Aerospace Engineering department.

a complete model of the discharge of ECR plasma thrusters and to perform parametric investigations, both to improve the current understanding of the complex phenomena within the thruster as well as to support the development of the prototype. SURFET is composed of two main parts: (i) HYPHEN,[14–17] a novel two-dimensional axisymmetric hybrid PIC/fluid model to solve for the internal plasma transport, and(ii) and ATHAMES[18] (Axisymmetric Time Harmonic Maxwell's Equations Solver), a full-wave, finite element (FE) formulation of the electromagnetic field-plasma problem in the frequency domain with both axisymmetric[19, 20] and planar capabilities, to model the RF-coupling present in ECR thrusters.

Understanding the operation of the ECRT requires understanding multiple physical mechanisms such as plasma-wave interaction, plasma-wall interaction, turbulence, etc, which nowadays lack a predictive model. The plasma-wave interaction problem is essential to ECR thrusters but it is also key for other applications in fusion tokamaks,[21, 22] for ECR ion source plasmas[23] and plasma etching.[24] The physical phenomena governing plasma-wave interaction, wave propagation and absorption in ECR plasmas has been substantially investigated.[25–29] Methods used for ECR simulation as beam/ray tracing algorithms[30, 31] are valid whenever the WKB condition is fulfilled (i.e. wavelengths are negligible compared to gradient lengths in the refractive index). This excludes the vicinity of resonances and cutoffs. Furthermore, as the thruster characteristic length is often comparable the wavelengths, a more adequate approach is required. That is the full-wave approach, that obtains solutions of Maxwell's equations directly in the simulation domain, either in time domain[32, 33] or frequency domain.[34, 35]

An explanation of the code structure with a brief description of the modules is detailed in section II. The physical and numerical models of ATHAMES are described in section III. Section IV shows the results of a self-consistent simulation using the thruster configuration of the prototype being developed in MINOTOR H2020 at ONERA. Finally conclusions are withdrawn of the present research and future work is explained in section V.

II. Self-consistent model and code structure

The SURFET code is composed of four different modules: (i) PIC-heavy species module, (ii) The electron-fluid module, (iii) Magnetic nozzle (MN) module, and the (iv) Electromagnetic (EM) wave module. The first two modules describe the transport of the plasma species inside the thruster and constitute the hybrid PIC/fluid/MonteCarlo HYPHEN code, presented in detail in Refs. 14–17. The third, DIMAGNO, describes the plasma expansion outside the chamber. The fourth module, ATHAMES, models the electromagnetic problem and the deposition of power in the plasma.

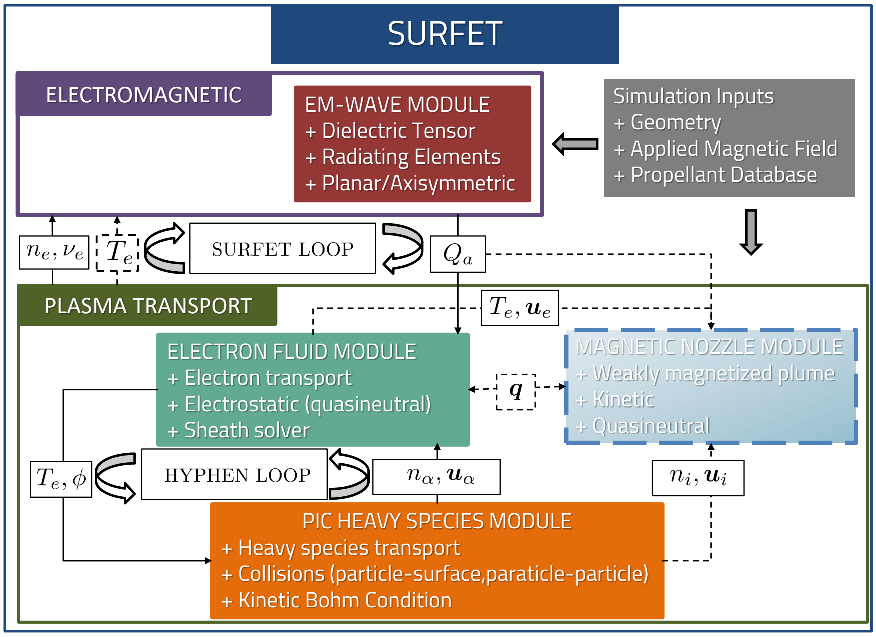

Figure 1: SURFET overall structure

The four modules interact with each other through a set of well defined inputs and outputs. The three transport modules provide to the EM-wave module the electron density and collisionality. In turn, the EM-wave module provides the power absorption map to the transport modules. These four modules together comprise the simulation loop that is executed until stationary conditions are reached.

An important remark is that every module operates on a different mesh generated in the simulation domain as a result of the different requirements implied in their models. A structured mesh is used by the PIC heavy species module (referred to as the PIC-mesh hereafter), a non-structured magnetic field aligned mesh (MFAM) for the electron module, a MN mesh generated with the method of characteristics as part of the solution, and a non-structured highly refined mesh for the electromagnetic fields in the chamber. Therefore, all modules have to go through an interpolation routine every time they communicate with each other. Specifically, a Gaussian filter is used for properties smoothing that are interpolated from the MFAM to the finer EM-mesh. Additionally, an spatial anti-aliasing algorithm is applied to the power absorption when interpolated to the MFAM. The algorithm averages the radially weighted power absorption of all the EM-mesh nodes contained at each MFAM cell.

A. Plasma transport modules

The physical and numerical algorithms of the internal transport modules are briefly discussed here; for a full description of the HYPHEN modules, the interested reader is referred to references 14–17, 36, 37.

The PIC module used in these simulations was developed by A.Domínguez-Vazquez.[15, 38–40] This model can be split in particle-wise and mesh-element-wise algorithms (i.e. applied to each particle or mesh-element). The particle-wise algorithms perform (*i*) interpolation of electrostatic and magnetostatic fields (*ii*) macroparticle trajectory integration through a leapfrog scheme, (*iii*) detection of macroparticles crossing PIC mesh surface elements, (*iv*) macroparticle sorting in multiple lists per population, and (*v*) particle removal for those particles that have left the simulation domain. As for the mesh-element-wise algorithms, they implement the different collisions experienced by the heavy species (e.g. ionization collisions) (*i*) volumetric weigthing of sorted macroparticles to obtain the macroscopic magnitudes, (*ii*) population control of the simulated heavy species to maintain the number of macro-particles per cell within a specified interval in stationary conditions.

The electron fluid module has been discussed in Refs. 41 and 37. More details of the works of the module can be found in.[16, 17] Here we only provide a brief description of the key aspects of the module. The electron-fluid module is composed by two systems. A continuity-momentum solver and an energy equation solver. As the modules are coupled together, an iterative approach is implemented, where each module is called sequentially in order.

Regarding the first module, charge conservation is modelled, where the ion currents are obtained from the PIC heavy species module. The electron current is computed from a generalized Ohm's law obtained from a diffusive model (i.e. inertia is disregarded) of the electron momentum equation. The collisions with all other species are retained and the equation is projected in the magnetic local axis defined by the direction parallel to the magnetic field $\mathbf{1}\parallel$, the azimuthal direction $\mathbf{1}\theta$ and the perpendicular to them $\mathbf{1}\top$. The method uses a thermalized potential instead of solving directly for ϕ. This choice is motivated by the ill-conditioned character of the system for solutions using ϕ as the variable in our problem (see Ref.37). As the energy equation is modelled (i.e. without the use of a polytropic closure for the electrons), the thermalized potential Φ proposed for the generalized case as

$$\Phi = \phi - \frac{T_e}{e} \ln \frac{n_e}{n_{e0}} \tag{1}$$

where ϕ is the electric potential, T_e is the electron temperature, and n_e and n_{e0} are the electron densities and the nominal value. In this solver the conservation equation is charge conservation and the state law is the definition of the electron current.

Regarding energy conservation, a closure equation for the heat flux is used to obtain a system that solves for the electron temperature (or pressure) and the heat flux. The energy conservation modelled is the internal energy equation:

$$\frac{\partial}{\partial t}\left(\frac{3}{2} n_e T_e\right) + \nabla \cdot \left(\frac{5}{2} n_e T_e \boldsymbol{u}_e + \boldsymbol{q}_e\right) = \boldsymbol{u}_e \cdot \nabla p_e + \sigma_e^{-1} \boldsymbol{j}_e \cdot (\boldsymbol{j}_e + \boldsymbol{j}_c) + Q_e - \frac{1}{2} m_e u_e^2 S_e + Q_a, \tag{2}$$

where $\boldsymbol{q}_e, \boldsymbol{j}_e$, $\boldsymbol{u}_e$, and p_e are the electron heat flux, current density, fluid velocity, and pressure and $\boldsymbol{j}_c = e n_e \sum_{s \neq e} \nu_{es}/\nu_e \boldsymbol{u}_e$ is the equivalent current for species s. In Eq.(2), S_e is the plasma production rate, Q_e

contains the effects due to inelastic collisions of ionization and excitation, and Q_a is the power absorption due to plasma-wave interaction. This term is computed by the EM-wave module (see section III). The heat flux is modelled with a generalized Fourier's law as

$$0 = -\frac{5p_e}{2e}\nabla T_e - \boldsymbol{q}_e \times \boldsymbol{B} - \frac{5p_e\sigma_e^{-1}}{2}\left(\boldsymbol{j}_e + \boldsymbol{j}_c\right) - en_e\sigma_e^{-1}\boldsymbol{q}_e. \tag{3}$$

which constitutes a state law for the electron heat flux (i.e. solving for $\boldsymbol{q}_e$ in Eq.(3)).

Both solvers substitute each state equation in their corresponding conservation laws, which are then discretized using a Finite Volume Method (FVM). The FVM integrates all quantities per cell and creates a system that solves for the thermalized potential in the case of the continuity and momentum solver and for the electron temperature (or pressure) in the case of the energy solver.

Several types of boundary conditions are considered in the problem. The boundary surfaces that let the plasma exit the domain 'freely' are defined as 'free-loss' surfaces. In these boundaries the condition for the currents is that the local total current density normal to the boundary is equal to zero. As for the heat flux, a null normal heat flux is imposed. Theses boundary conditions are also imposed for the symmetry axis and for the dielectric walls.[17]

Additionally in the case of a dielectric wall, the boundary condition implemented is that for Boron Nitride (BN). This boundary condition additionally uses a sheath model[16, 42] that given the current of ions (in that case equal to the electrons) and the electron density and temperatures to compute the increase of potential in the sheath and also a condition on the boundary electron heat flux.

In the case of a conductor the sheath model requires an iterative algorithm since the sheath depends on the electron current and that is not equal to the ion current in this type of sheath.

An important remark in this model is that several mechanism to limit the confinement of the electron species (i.e. limiting the hall parameter) in the thrusters are implemented in this model. One of them is to increase the conductivity with a factor proportional to the cyclotron frequency. Another model imposes a limiter in the maximum hall parameter achieved in the simulation. The motivation of this limitation have both physical (i.e. turbulence and anomalous transport) and numerical (e.g. ill-conditioned linear systems) motivations.

III. The EM-wave module

The EM-wave module is a full-wave FE two dimensional axisymmetric code that solves Maxwell's equations in frequency domain. The plasma model used is a cold-plasma dielectric tensor description that retains collisional effects. The code takes as inputs the electron density and collisionality maps obtained by the hybrid module together with the thruster geometry, the excitation mechanism and applied magnetic field configuration. The code returns the electromagnetic wave fields and power absorption maps. The FE discretization is implemented with the open-source FE library MFEM.[43]

Due to the novelty of this module, the physical and numerical models used are described in further detail compared to the hybrid module.

Guided by the investigation on the accuracy of full-wave numerical schemes shown in Ref. 44, a 2D full-wave Galerkin's FE formulation based on mixed basis of shape functions was selected to solve the curl-curl equation (12) in the meridian plane. This choice was based on two main considerations.

Firstly, FE methods do not rely on structured grids. Thus, FE allows for proper treatment highly nonuniform problems and complex geometries. This enables a finer description of the ECR region, which features a rapid change in the propagation properties, thus requiring non-uniform complex refinement to be capable of characterizing the minimum wavelengths of the problem. The open-source software GMSH[45] is used as mesher.

Secondly, the use of curl-curl formulation for Maxwell's equations with respect to first-order Maxwell's curl equations provides with several advantages and drawbacks. On the one hand, double curl formulation allows to solve independently for the wave electric field in all the mesh nodes and requires no treatment for non-self-adjoint first order derivatives as in Ref. 46. On the other hand, it is known[47] that the double curl equations has more solutions than first order equations (i.e. spurious solutions) under certain circumstances. In FE this is treated either by penalizing the non-zero divergence as in Ref.,[48] or using Nédélec edge element method, which solves for the difficulties of spurious solutions.[49–51] The latter is limited to divergence-free cases, and provides hindered computational efficiency and accuracy[49] with respect to nodal element formulation, although the latter requires appropriate treatment of singularities in Perfect Electric Conductor (PEC) corners.

A. Physical model

The propagation of electromagnetic waves is governed by Maxwell equations, i.e.,

$$
\begin{aligned}
\nabla \times \boldsymbol{E} &= -\frac{\partial \boldsymbol{B}}{\partial t}; & (4)\\
\nabla \cdot \boldsymbol{E} &= (\rho_p + \rho_a)/\varepsilon_0; & (5)\\
\nabla \times \boldsymbol{B} &= \mu_0 \varepsilon_0 \frac{\partial \boldsymbol{E}}{\partial t} + \mu_0 \left(\boldsymbol{j}_p + \boldsymbol{j}_a\right); & (6)\\
\nabla \cdot \boldsymbol{B} &= 0, & (7)
\end{aligned}
$$

where $\boldsymbol{j}_p$, ρ_p represent the plasma electric current density and charge density that result from the all charged species. The terms $\boldsymbol{j}_a$, ρ_a represent the generic forcing terms used to describe the presence of electric current density and charge density of radiating elements.

The solution of equations (4) to (7) must be obtained together with a plasma model for the plasma current and charge densities $\boldsymbol{j}_p, \rho_p$ to close the problem.[52, 53] Fourier analysis is used to transform the Maxwell problem into the frequency domain. The plasma modeled us is the cold plasma model, so that its response to the wavefields is linearized to maintain a relative dielectric tensor description of the medium (albeit anisotropic and complex) $\boldsymbol{\kappa}$, which is a function of the excitation, plasma, and cyclotron frequencies, as well as the propagation direction. Thus the two component plasma dielectric tensor[52] can be expressed in the local magnetic basis as

$$
\kappa = \begin{bmatrix} S & -iD & 0 \\ iD & S & 0 \\ 0 & 0 & P \end{bmatrix}, \quad
\left\{
\begin{array}{ll}
S & = 1 - \sum\limits_k \frac{\omega_{ps}^2 (\omega + i\nu_k)}{\omega\left[(\omega + i\nu_k)^2 - \omega_{ck}^2\right]}, \\
D & = \sum\limits_k \frac{s_k \omega_{ck} \omega_{pk}^2}{\omega\left[(\omega + i\nu_k)^2 - \omega_{ck}^2\right]}, \\
P & = 1 - \sum\limits_k \frac{\omega_{pk}^2}{\omega(\omega + i\nu_k)}
\end{array}
\right. \qquad (8)
$$

where $k = e, i$ for electrons and ions and thus $s_e = -1, s_i = +1$. Furthermore ω_{ck}, ω_{pk} and ν_k are the plasma, cyclotron, and damping frequency of species k, respectively. Moreover P, S and D stand for the "parallel", "sum" and "difference" so that

$$
S = \frac{1}{2}\left(R + L\right), \qquad D = \frac{1}{2}\left(R - L\right). \qquad (9)
$$

where R (i.e."right-hand") & L (i.e."left-hand") refer to the sense of their respective polarization. Overall, the triplet

$$
L = 1 - \sum_k \frac{\omega_{pk}^2}{\omega\left(\omega + i\nu_k - s_k\omega_{ck}\right)}, \; R = 1 - \sum_k \frac{\omega_{pk}^2}{\omega\left(\omega + i\nu_k + s_k\omega_{ck}\right)}, \; P = 1 - \sum_k \frac{\omega_{pk}^2}{\omega\left(\omega + i\nu_k\right)}, \qquad (10)
$$

defines the dispersion relation of the right-hand and left-hand polarized waves and plasma oscillations. In the microwave regime (GHz range) the ion response constitutes a negligible contribution to the dielectric tensor and can be safely neglected in first approximation (i.e. $\omega \gg \omega_{ci}, \omega_{pi}$). For electrons, the plasma and cyclotron frequencies are

$$
\omega_{pe}^2 = \frac{e^2 n_0}{\epsilon_0 m_e} \quad \text{and} \quad \omega_{ce} = \frac{e B_0}{m_e}. \qquad (11)
$$

The model retains the relevant physics to study many of the wave-plasma interaction problems, including propagation, cutoffs, and accessibility.[52] It also allows identifying the fundamental and secondary resonances.

The hermitian part of the dielectric tensor is related with wave propagation. The antihermitian part introduced with ν_e is related with wave damping and power deposition into the plasma (see subsection C).

The validity of the inclusion of the effective collisionality in the modelling of ECR resonances is shown in Ref. 44. In that analysis, we showed that the actual value of the damping constant does not modify substantially the major output of the wave code, which is the power absorption. Regardless of the damping mechanism (kinetic, collisional), a small value of the collisional parameter suffices to absorb power, without affecting either the transmitted or the reflected amount of power through the resonance. The impact of this parameter is related essentially only to the thickness of absorption layers and the magnitude of the fields near resonance. This is also present in the power absorption results shown in Figs. 9e and 9f.

Combining Eqs. (4) and (6) allows eliminating the wave magnetic field $\boldsymbol{B}$, one finds inhomogeneous Maxwell's wave equation also referred to as the double-curl wave-equation for the electric field. In frequency domain and modelling plasmas response with the dielectric tensor $\bar{\bar{\kappa}}$, the equation reads:

$$\nabla \times \left(\nabla \times \hat{\boldsymbol{E}}\right) - k_0^2 \boldsymbol{\kappa} \cdot \hat{\boldsymbol{E}} = i\omega\mu_0 \hat{\boldsymbol{j}}_a, \tag{12}$$

where $\boldsymbol{E} = \Re[\hat{\boldsymbol{E}} \exp\left(-i\omega t\right)]$, and k_0 is the wave number in vacuum. The linearization applied to the plasma response in Maxwell's equations allows for the use of the superposition principle. Thus, in case multiple frequencies are excited the complete solution is the addition of each solution for each individual frequency.

B. Mathematical model

Applying the inner product of the complex weighting functions $\boldsymbol{W}$ with Eq. (12), and integrating by parts in the domain Ω, one finds the weak form of Eq.(12) given in Ref.49 :

$$\int_\Omega \left[\left(\bar{\bar{\mu}}_r^{-1}\nabla \times \hat{\boldsymbol{E}}\right) \cdot \left(\nabla \times \hat{\boldsymbol{W}}^*\right) - \left(k_0^2 \bar{\bar{\kappa}} \hat{\boldsymbol{E}}\right) \cdot \hat{\boldsymbol{W}}^*\right] dV + \int_{\partial\Omega} \left[\hat{\boldsymbol{n}} \times \left(\nabla \times \hat{\boldsymbol{E}}\right)\right] \cdot \hat{\boldsymbol{W}}^* dS = i\mu_0\omega \int_\Omega \hat{\boldsymbol{j}}_a \cdot \hat{\boldsymbol{W}}^* dV, \tag{13}$$

where $\Omega, \partial\Omega$ are the simulation domain and its enclosing boundary, $\hat{n}$ is outward unitary normal vector to $\partial\Omega$, $\boldsymbol{W}, \boldsymbol{E}$ are the test (i.e. weighting) and trial (i.e. shape) functions respectively. Following the classical Galerkin's approach, the same functional spaces are used for the discretization of both $\hat{\boldsymbol{W}}, \hat{\boldsymbol{E}}$. The second term of Eq. (13) represents the boundary conditions closing domain Ω. These boundaries $\partial\Omega$ can be split into:

$$\partial\Omega = \partial\Omega_D + \partial\Omega_N + \partial\Omega_C \tag{14}$$

which represent homogeneous Dirichlet (i.e. PEC), homogeneous Neumann (i.e. perfect magnetic conductor, PMC) and Cauchy. The latter allows to define $\hat{\Psi}$ for either an absorbing boundary condition or a waveport. The boundary conditions on the fields are:

$$\hat{\boldsymbol{n}} \times \hat{\boldsymbol{E}} = 0 \quad \text{on } \partial\Omega_D, \tag{15}$$

$$\hat{\boldsymbol{n}} \times \left(\nabla \times \hat{\boldsymbol{E}}\right) = 0 \quad \text{on } \partial\Omega_N, \tag{16}$$

$$\hat{\boldsymbol{n}} \times \left(\nabla \times \hat{\boldsymbol{E}}\right) + i\gamma \hat{\boldsymbol{n}} \times \hat{\boldsymbol{n}} \times \hat{\boldsymbol{E}} = \hat{\boldsymbol{\Psi}} \quad \text{on } \partial\Omega_C. \tag{17}$$

Thus, Eq. (13) is expressed as:

$$\begin{aligned} &\int_\Omega \left[\left(\nabla \times \hat{\boldsymbol{E}}\right) \cdot \left(\nabla \times \hat{\boldsymbol{W}}^*\right) - \left(\boldsymbol{\kappa} \hat{\boldsymbol{E}}\right) \cdot \hat{\boldsymbol{W}}^*\right] dV + \\ &\quad + \int_{\partial\Omega_C} \left[i\gamma \left(\hat{\boldsymbol{n}} \times \hat{\boldsymbol{W}}^*\right) \cdot \left(\hat{\boldsymbol{n}} \times \hat{\boldsymbol{E}}\right) + \hat{\boldsymbol{\Psi}} \cdot \hat{\boldsymbol{W}}^*\right] dS = i \int_\Omega \hat{\boldsymbol{j}}_a \cdot \hat{\boldsymbol{W}}^* dV \end{aligned} \tag{18}$$

For the simulation of body of revolution domains, the simulation domain is expressed in cylindrical coordinates and harmonic oscillation in θ coordinate is assumed for all quantities. The electric field can be expressed as:

$$\hat{\boldsymbol{E}}(z, r, \theta) = \sum_{m=-\infty}^{\infty} \tilde{\boldsymbol{E}}^{(m)}(r, z) e^{im\theta}. \tag{19}$$

Due to its periodicity, contrary to the 2D planar model, the mode number (i.e. m) is no longer a real number but an integer number. The discretization of $\tilde{\boldsymbol{E}}^{(m)}$ and $\tilde{\boldsymbol{\Phi}}^{(m)}$ in the axisymmetric case depends on the mode number m to satisfy the following boundary conditions at the symmetry axis:

$$\tilde{E}_r^{(0)} = \tilde{E}_\theta^{(0)} = 0, \tag{20}$$

$$\tilde{E}_r^{(\pm 1)} = \mp i \tilde{E}_\theta^{(\pm 1)} = 0, \quad \tilde{E}_z^{(\pm 1)} = 0, \tag{21}$$

$$\tilde{E}_r^{(m)} = \tilde{E}_\theta^{(m)} = \tilde{E}_z^{(m)} = 0, \quad |m| > 1. \tag{22}$$

This approach is explained in Refs.19, 50, and the discretizations needed are:

$$\tilde{\boldsymbol{E}}^{(m)} = \begin{cases} \sum_{i=1}^{N_{\text{edge}}} \boldsymbol{N}_i\left(r,z\right) e_{t,i}^{(m)} + \mathbf{1}_\theta \sum_{i=1}^{N_{\text{node}}} N_i\left(r,z\right) e_{\theta,i}^{(m)} & m=0 \\ \sum_{i=1}^{N_{\text{edge}}} r\boldsymbol{N}_i\left(r,z\right) e_{t,i}^{(m)} + \left(\mathbf{1}_\theta \mp i\mathbf{1}_r\right) \sum_{i=1}^{N_{\text{node}}} N_i\left(r,z\right) e_{\theta,i}^{(m)} & m=\pm 1 \\ \sum_{i=1}^{N_{\text{edge}}} r\boldsymbol{N}_i\left(z,r\right) e_{t,i}^{(m)} + \mathbf{1}_\theta \sum_{i=1}^{N_{\text{node}}} N_i\left(z,r\right) e_{\theta,i}^{(m)} & |m|>1 \end{cases} \tag{23}$$

where $\boldsymbol{N}_i(r,z)$ are the Nédélec vector basis functions whose associated degree of freedom (i.e. unknown expansion coefficient) is $e_{t,i}^{(m)}$, and $N_i(r,z)$ are the nodal basis functions whose degree of freedom is $e_{\theta,i}^{(m)}$. These FEM expansions satisfy Eq. (20-22) with an homogeneous Dirichlet condition on E_θ for $m \neq \pm 1$ and otherwise natural boundary conditions (i.e. PMC). Additionally, due to axisymmetry one may write:

$$\nabla \times \hat{\boldsymbol{E}} = \left[\nabla \times \tilde{\boldsymbol{E}}_t + \frac{im}{r}\mathbf{1}_\theta \times \tilde{\boldsymbol{E}}_t - \frac{\mathbf{1}_\theta}{r} \times \nabla\left(r\tilde{E}_\theta^{(m)}\right)\right] e^{im\theta}, \tag{24}$$

where $\tilde{\boldsymbol{E}}_t$ and $\tilde{E}_\theta$ are the electric fields tangential and normal to the zr plane. Thus, Eq. (18) needs to be modified accordingly to build up the system of equations.

As the thruster geometry and fields (i.e. the coaxial) excited by the coaxial are axisymmetric, the case of interest for the ECR thrusters is the mode $m = 0$. All the results shown in this work are for the purely axisymmetric fields.

The excitation of the coaxial is performed through a lumped port. A radial current is used to excited a domain between the outer and inner conductors and a axial length $L_p << \lambda_0$, being λ_0 the wavelength in vacuum. This excitation combined with a PMC boundary condition applied to the inlet of the coaxial allows to excite the transverse electromagnetic field (TEM) in the coaxial, and as a result model the excitation of the entire simulation domain.

The MN is not investigated in this work. The electromagnetic fields computed by the EM-wave module shown in Sec.IV are for the near fields that appear in the near-plume region. The results are obtained using the quantities obtained with HYPHEN.

IV. Self-consistent simulations

A. Geometry, magnetic field configuration and operational parameters

The ECR thruster geometry used for this simulations is that of the prototype being matured at ONERA, shown in Fig.2. The simulation domain consists of a coaxial, a thruster chamber and a plasma plume. We will differentiate two simulation domains; one for the hybrid module (Domain H) and another for the electromagnetic wave module (Domain W). These domains have specific boundaries:

1. Domain H: [S1,S2,S3,S45,S5,S6,S7*,S78,S11].
2. Domain W: [S1,S2,S3,S4,S5,S6,S7,S8,S9, and S10]. Observe that it includes the coaxial line that feeds EM power to the thruster.

The boundary conditions imposed for each module are described hereinafter.

1. *Boundary conditions of the transport module*

The prototype at ONERA uses a BN coating on the thruster walls including the antenna. Therefore from the point of view of the transport the antenna is modelled as a BN dielectric wall (i.e. surfaces S1,S6,S7,S11). Furthermore, current model assumes that the injection surface is a porous injector made of BN (S78). Additionally, this surface injects a neutral mass flow rate $\dot{m}$. As all these surfaces are dielectrics, the boundary conditions used are that the total current is zero and that the heat flux is that given by the sheath model. For the heavy species neutral reflection is imposed and ion recombination.

The free-loss surfaces S3 and S45 assume that at the plume boundaries of the simulation domain so that the normal electron heat flux and total current are zero. This condition is more adequate the further the truncation of the domain. For the ions and neutrals a particle removal is executed having computed their contribution to the fluxes to the walls.

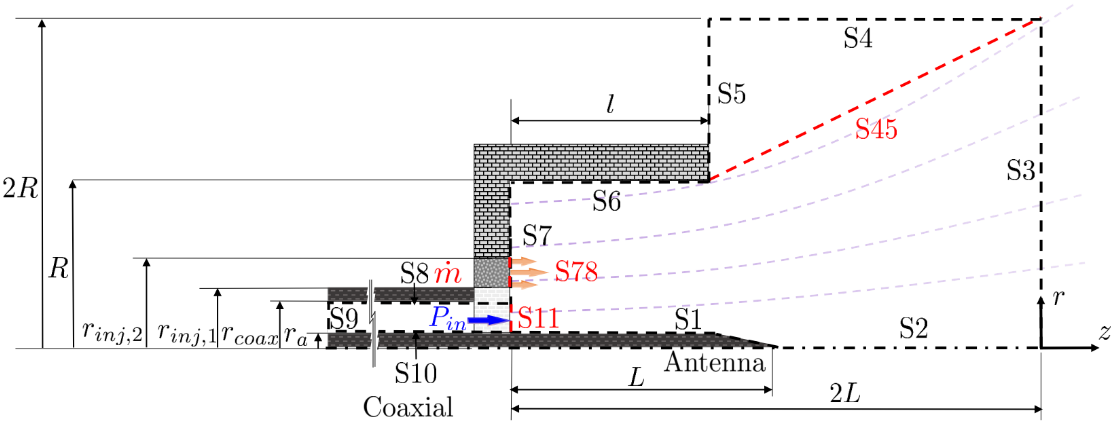

Figure 2: Schematic of the simulation domain, boundary surfaces and geometrical details of the coaxial ECR thruster simulated. Surfaces (S) define the boundaries of the domain. Geometrical dimensions are expressed in Tab.1.

The motivation of surface S45 arises from the magnetic configuration of the thruster, shown in Fig.3a. Perpendicular transport is not enough to fill the region above the last magnetic field line exiting the thruster chamber. As this resulted in an insufficient number of particles per cell at that region, the domain was truncated there to limit PIC noise in the simulations. The plasma properties used by the EM-wave module at the region between surfaces S4,S5, and S45, are extrapolated from the values inside the domain using a linear method.

Finally, axisymmetric boundary conditions are imposed in S2. This implies an specular reflection for neutrals and ions, and zero total current density and electron heat flux equal normal to the axis.

2. Boundary conditions used by the electromagnetic module

PEC are imposed both at the inner and outer conductors of the coaxial (i.e. S8 and S10), and at every thruster chamber wall including the antenna (i.e. S1,S6,S7) and surface S5 which is part of the Domain W. The latter is justified given the negligible thickness of the BN coating and the dominance of a PEC condition beneath the coating.

The boundary conditions used for the plume (i.e. S3 and S4) are imposed to be natural boundary conditions of the weak formulation. The intention was to allow tangential fields to these surfaces. Such condition will be substituted by an absorbing boundary condition or a perfectly matched layer in future simulations.

The injection surface for the coaxial port (i.e. S9) is set with a PMC boundary condition. This condition allows to excite the TEM mode in the coaxial with the combination of a radial current in the lumped element.

Downstream the thruster chamber exit, the plume is truncated at surfaces (S4) which fulfill free loss boundary conditions.

The symmetric axis (S5) uses the corresponding axisymmetric boundary conditions explained in Section

Parameter	Name	Units	Value
L	Antenna length	cm	2
r_a	Antenna radius	cm	0.115
l	Outer conductor length	cm	1.51
R	Outer conductor radius	cm	1.375
$r_{inj,2}$	Injection surface outer radius	cm	0.688
$r_{inj,1}$	Injection surface inner radius	cm	0.459
r_{coax}	Coaxial outer radius	cm	0.3

Table 1: Geometrical parameters used for the sample simulations.

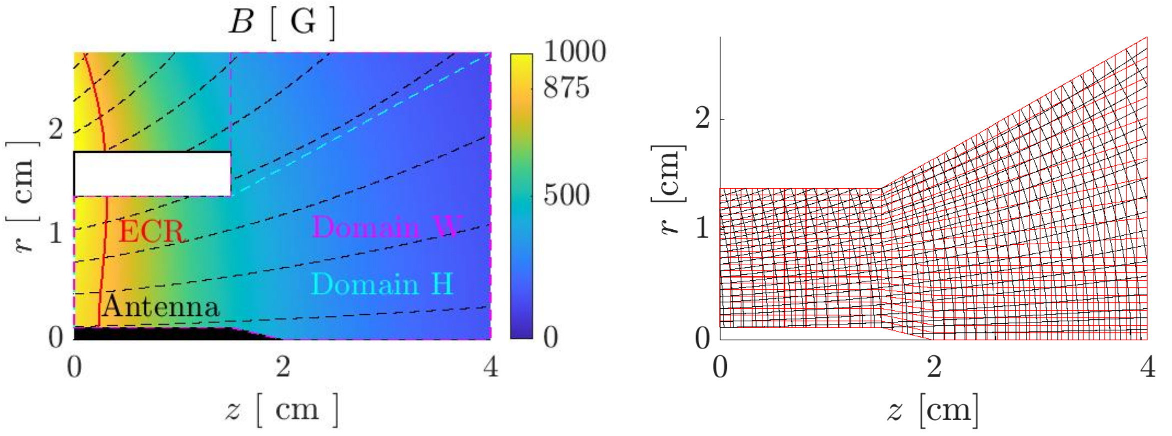

(a) **(b)**

Figure 3: a) Applied magnetic field on the ECR thruster at ONERA. Black lines represent magnetic field lines and white lines are magnetic intensity isolines. The colorbar represents the magnetic field intensity. b) In red the PIC mesh and black the MFAM.

The magnetic field intensity and topology (see Fig.3a) is designed so that the ECR region spans radially at $z \approx 2.4$mm. The PIC-mesh and MFAM used for this simulation are shown in Fig.3b generated to have similar cell-sizes in the domain.

B. Simulation results

Parameter	Name	Units	Value
f	Excitation frequency	GHz	2.45
$\dot{m}$	Neutral mass flow rate	mgs^{-1}	0.2
P_a	Power deposited	W	30
u_{inj}	Propellant injection velocity	ms^{-1}	300
T_{inj}	Propellant injection temperature	eV	0.02
α	Propellant type	-	Xe

Table 2: Parameters used for the two simulation scenarios.

Simulation settings shown in Tab.3 have been chosen to be similar to the real operational parameters of the prototype. The hall parameter has been limited to a maximum of 50 in this simulation. Simulation converges around $t = 2$ ms of simulation as shown in Fig. 4. There, the time evolution of relevant thruster performance parameters are shown. The simulation starts with an initialization with an isothermal model with a Boltzmann relation for the electron population. During this stage, the electron fluid module is not used, neither is the wave module. After this initialization of 1 ms, a first step using the complete electron fluid model is performed, assuming a uniformly distributed power absorption profile equivalent to 30 W for a period of 0.25 ms. Afterwards, several coupled iterations with the wave module are applied. As can be noticed, after two required for the convergence of the simulation, each during 0.25 ms. Simulation results shown are of the converged solution at $t = 3.5$ms. The peaks shown in Fig.4 for the divergence efficiency (specially near $t = 3$s) could be explained by the numerical noise associated to fast ions exiting radially the simulation domain close to the node connecting surfaces S45 to S6. At this region the electric fields are radial and with a magnitude of the order of 6000 V/m in our simulation.

T_{e0} [eV]	n_0 [m^{-3}]	j_0 [Am^{-2}]	S_0 [m^{-3}s^{-1}]	$Q_{a,0}$ [Wm^{-3}]	c_{s0} [ms^{-1}]	E_0 [Vm^{-1}]	q_0 [Wm^{-2}]
20	3.81×10^{17}	234	1.46×10^{23}	691115	3834	2000	4.68×10^3

Table 3: Normalization parameters.

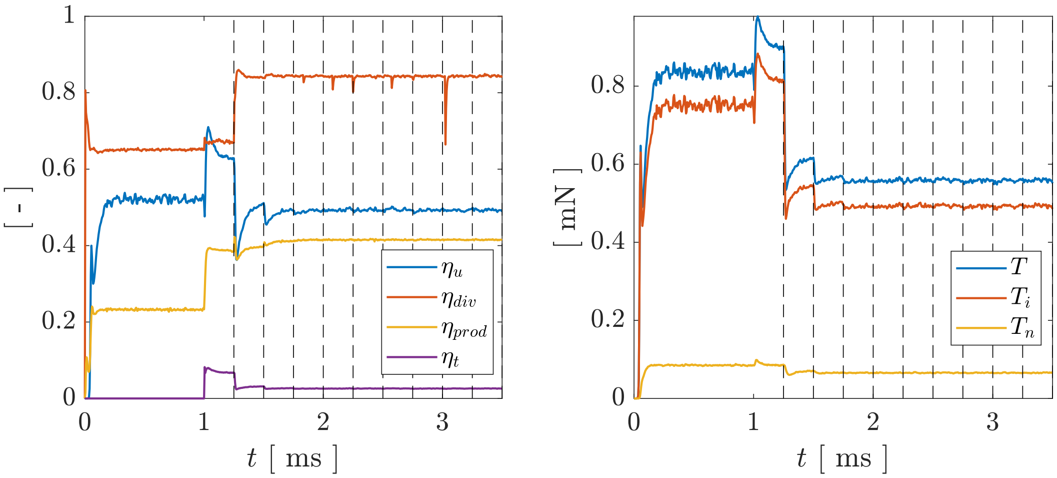

Figure 4: Evolution with simulation time of the thruster performance parameters. The power absorption is updated by the wave module every time-step marked as a vertical dashed line.

Parameter	Name	Units	UC3M SURFET	ONERA[13]
T	Thrust	mN	0.558	0.850
I_{sp}	Specific impulse	s	285	429
I_i	Ion current	A	0.072	0.062
η_t	Thrust efficiency	%	2.6	3.5
η_u	Utilization efficiency	%	49	45
η_{prod}	Production efficiency	%	42	[-]
η_{div}	Divergence efficiency	%	84	70
η_{en}	Energy efficiency	%	14	16
ϵ_{ex}	Excitation losses	-	0.05	[-]
ϵ_{ion}	Ionization losses	-	0.07	[-]
ϵ_{mat}	Material wall losses	-	0.74	[-]
VSWR	Voltage ratio	-	1.75	∼ 1.58
$\lvert\Gamma\rvert$	Voltage reflection ratio	-	0.27	∼ 0.224
P_r	Power reflected	%	7.41	∼ 5.0

Table 4: Comparison of performance parameters between simulations and measurements.

Tab.4 shows a comparison between the performances obtained by the self-consistent simulation and the ones obtained by ONERA with its coaxial prototype for the same operational parameters. The efficiencies are defined as

$$\eta_u = \frac{\dot{m}_{i,fl}}{\dot{m}}, \quad \eta_{prod} = \frac{\dot{m}_{i,fl}}{\dot{m}_{i,total}}, \quad \eta_{div} = \frac{P_{i,fl,z}}{P_{i,fl}}, \quad \text{and,} \quad \eta_t = \frac{T^2}{2\dot{m}P_a}, \tag{25}$$

where $\dot{m}_{i,fl}$ is the ion mass flow through free loss surfaces (i.e. S45 and S3), $\dot{m}_{i,total}$ is the total ion mass flow through boundaries, $P_{i,fl}$ and $P_{i,fl,z}$ are the total and axial powers of the ions exiting the domain through free loss surfaces, and P_a is power deposited in the thruster.

The total energy balance for all species yields

$$P_a = P_{fl} + P_{exc} + P_{ion} + P_{wall} \tag{26}$$

where P_{fl} is the integrated power flux through free-loss surfaces, P_{exc} and P_{ion} are the powers spent in both excitation and ionization, and P_{wall} is the power lost through the walls. Normalizing all terms in (26) by P_a, we obtain η_{fl}, ϵ_{exc},ϵ_{ion}, and ϵ_{wall}.

The VSWR is computed as the ratio of the maximum and minimum values of the radial electric field that is obtained in the coaxial at a specific radius. From those values the magnitude of the reflected voltage and power can be computed as:

$$|\Gamma| = \frac{VSWR-1}{VSWR+1}, \quad \text{and} \quad P_r = |\Gamma|^2. \tag{27}$$

The overall performances obtained by the simulations show fair agreement with the experimental results. As can be seen the coaxial design shows efficient power coupling with the plasma as the power reflected is only around a 7%. A large amount of power is lost through the walls. The magnetic field configuration with lines that intersect the lateral wall could be a cause for this result. Furthermore, note that the amount of energy used for ionization is only a 5% of the total. Given the utilization efficiency is 49% reported here, this might indicate that there is still room of improvement for the ionization strategy chosen (i.e. resonance location, electromagnetic power feeding mechanism, injector location, etc).

The maps of the properties obtained in the meridional plane are shown in Figs. 5 and 6 for the transport module and in Figs. 7 through 9e for the EM-wave module.

1. Transport module results

The plasma potential shown in Fig.5a shows monotonically decreasing potential downstream the thruster exit due to the expansion. Inside the thruster chamber, due to the nonuniform character of the plasma densities in the chamber, two potential peaks appear near the backplate and decay radially to the walls. The high magnetic confinement exhibited at these regions results in an electric field (see Fig.5b) that ensures the fulfillment of quasi-neutrality balancing the fluxes of ions to that of the electrons. An additional effect of the magnetic confinement is the asymmetry between the radial evolution of the potential for the inner and outer thruster walls. Whereas the potential decreases rapidly approaching the antenna surface, this effect is more moderate for the outer wall. We attribute this to the divergent character of the magnetic field lines, that produces that the outer wall is directly connected to the properties at the back-plate that are transported parallel to the magnetic field lines, contrary to the antenna. Furthermore note the electric fields found close to the antenna are of the order of 600Vm^{-1}. This result might explain the a high erosion experienced in the antenna.

The plasma density is represented in figure Fig.5c, where a maximum density of the order of 10^{18} m^{-3} is reached in the vicinity of the injector. The expansion downstream reaches plasma densities around $10^{16} m^{-3}$ in the near plume. Noteworthy is the radial profile of the density, which inside the chamber decreases close to the outer chamber wall and the inner wall (i.e. antenna) due to recombination at the walls. Downstream the thruster exit, the density rises moderately again for smaller radius. The latter can be explained by the presence of ionization in the vicinity of the antenna tip.

The density of neutrals (see Fig.5d) has its maximum of approximately $5 \times 10^{19} m^{-3}$ at the injection port and decreases rapidly filling the thruster chamber uniformly with plasma densities in the order of $5 \times 10^{18} m^{-3}$ that shows poor ionization of the plasma is achieved. This can be explained by the location of the maximum heating being close to the antenna and not to the injector and that the heating within the resonance region decreases rapidly two orders of magnitude with increasing the radius. The monotonically divergent character of the magnetic field lines (see Fig.3a) allows for an increased plasma density close to the outer wall, together with the transport of other quantities (i.e. particle fluxes, heat fluxes Fig.6e), resulting in increased plasma-wall interaction at that wall. This preliminary result might suggest that a different magnetic configuration with improved confinement would improve thruster performances.

Fig.5e shows the electron temperature, that reaches a maximum of 52 eV close to the antenna where the power absorption takes place (see Fig.5f). As the plasma is strongly magnetized, the electrons are nearly isothermal along each magnetic line (compare with Fig.3a) due to the dominant parallel conductivity. Furthermore the majority of the electromagnetic power is absorbed close to the antenna, with a maximum at the vicinity of the resonance. Further explanation is given in Subsec.C.

The ionization rate shown in Fig.5g exhibits a maximum of 1.43×10^{24} m^{-3}s^{-1} close to the injection and decreases rapidly with the distance from the injection port.

The ion velocity exhibits an acceleration exiting the thruster as expected, with the sonic velocity located just at the exit of the thruster for the maximum radius and extending up to $z = 4$cm for the axis. Noteworthy is the fact that the acceleration is steeper for the injector radius. Also note that Bohm condition on the ions is only fulfilled correctly at the antenna.

The ion currents in the meridional plane (see Fig.6a are maximum at a region located 3mm downstream the injector and directed radially. High current densities in the order of $200\mathrm{Am}^{-2}$ close to the outer wall. The ion current increases in the axial direction for increasing z reaching values in the order of $50\mathrm{Am}^{-2}$ but with a radial gradient in the intensity. Figure 6b shows that the electron currents are stronger than the ion currents, specially close to the antenna where the electrons exhibit high axial currents in the order of $1000\mathrm{Am}^{-2}$. Azimuthal electron currents are higher than the meridional electron currents and exhibit two different signs in the direction of this component of the current within the thruster chamber that can be explained by the pressure gradient changing sign with the radius. Furthermore, as all boundary conditions imposed require a zero current at the boundaries the total current density (see Fig.6c) exhibits loops so that the current is parallel to the boundaries at each boundary surface.

Regarding the tangential heat flux (see Fig.6e), the boundary conditions seem to be fulfilled adequately as the heat flux performs loops around the simulation domain. However the boundary conditions for the electron heatflux at the boundaries arise from an assumption. Further investigation on alternative methods is required. Note that the maximum electron heat fluxes are parallel to the antenna and are located close to the antenna as could be expected from the highly energetic character of the electron population in magnetic field lines. The azimuthal heat flux (see Fig.6f) exhibits strong variations and a change of sign that resembles the radial gradient in the electron temperature (see Fig.5e). When the gradient changes sign so does the azimuthal heat flux.

2. EM-wave module results

The CMA diagram[52] is a useful tool to analyze the different electromagnetic wave propagation and absorption regimes in a cold-plasma. Although this figure represents the collisionless cold-plasma two-species module, it has shown significant importance in the analysis of the results obtained by the EM-wave module. In Fig. 7 the colormap represents the different CMA regions existing in the plasma obtained by the plasma transport module with the applied magnetic field configuration imposed is specified. As it can be noticed in this ECRT simulation, all the regions for a cold-plasma with electron species are present in the simulation domain. The contour lines detail the location of the different cutoffs and resonances predicted by the CMA (i.e. cold-plasma model). The lines $R = 0$, $P = 0$ and $L = 0$ represent the different cutoffs that affect the propagating modes in the parallel direction. The line $S = 0$ in this case represents the boundary between region 2 and region 3 of the CMA diagram, and it is the so called upper hybrid resonance (UHR).

Note that whereas the location of the ECR region is fixed only by the magnetic field, the UHR region is determined by a combination of both the magnetic field and the plasma density. Noteworthy is the fact that the wave from the coaxial enters through a region 6 and 7 instead of through a region 8 as could be expected a priori. Focus has to be taken in the fact that the location of the resonance specifies the location of a dominant region 5 (i.e. evanescent for all EM propagation) downstream the thruster, if the density is above the critical plasma density at that point. In our case this density is of the order of 7×10^{16} m^{-3} for this excitation frequency, and this is the density exhibited at parallel mode cutoff line (P=0). As we desire dense plasma beams we assume that this region will be always there and will not allow EM power to be deposited far downstream. However, note as the plasma density decreases towards the antenna, it allows for the development propagating regions within a region close to it. Furthermore it has been noticed that for different plasma conditions the CMA is altered and again that the electromagnetic fields show that they are closely governed the CMA.

In Figs.8a, 8e, 9a the magnitude of the electric fields is detailed. The phase of the fields are depicted in 8c, 8g, 9a. Firstly, looking at the different components of the fields it is evident that the azimuthal fields that appear in the chamber are much smaller than the tangential fields. Furthermore the dominant fields in the thruster are radial electric fields located close to the antenna and extending through regions 6,7 and after the ECR 3 and 4. The axial fields are stronger close to the antenna tip and before the ECR resonance. At the resonances, the fields exhibit an increase of the fields.

As for the phases, it can be noticed that the phase exhibits sudden changes in the vicinity of the different lines described by the CMA diagram. In fact a small axial field wave-like pattern appears in region 4 close to the antenna tip.

An interesting electric field pattern appears upstream the ECR with an angle and exiting from the outer radius of the conductor. The phase of the fields before and after this line are clearly out of phase as can be seen in Figs.8c and Figs.8g.

The power absorption, which is the main result obtained by the EM-wave module is shown in Fig.9e.

As could be expected the power is principally absorbed in the vicinity of the ECR with a width that can be explained by the pressence of damping (see Ref.44). However some smaller contributions appear close to the antenna and far from the ECR. The motivation behind the location of the power close to the antenna is detailed in Subsec.C.

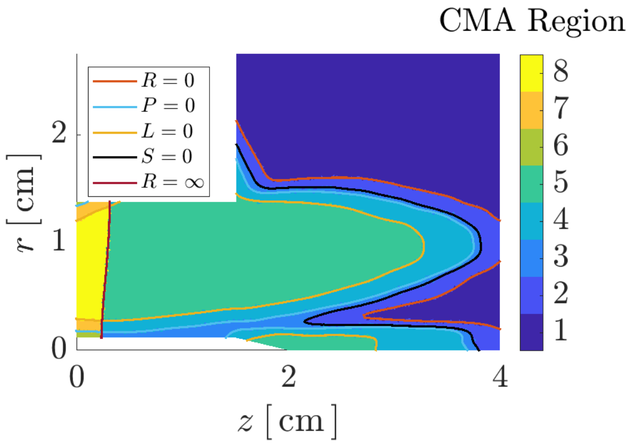

Figure 7: Different propagation and absorption regimes in the domain (regions of the CMA diagram).

C. Power deposition location

Qa absorption located close to the antenna can be explained from the definition of power absorption. Taking the dielectric tensor for a cold-plasma one can separate between the hermitian and the antihermitian part of the tensor. It results that the conductivity tensor arising from an hermitian dielectric tensor $\bar{\bar{\sigma}}^H$ does not deposit any power, independently of the electric fields. However, the addition of collisions to the cold-plasmas model adds an antihermitian part to the dielectric tensor. This tensor in the local magnetic axis where the third component is the direction parallel to the magnetic field, can be written as:

$$\bar{\bar{\kappa}}^A = \frac{1}{2}\left(\bar{\bar{\kappa}} - \bar{\bar{\kappa}}^*\right) = i \begin{bmatrix} \Im(S) & -i\Im(D) & 0 \\ i\Im(D) & \Im(S) & 0 \\ 0 & 0 & i\Im(P) \end{bmatrix} \tag{28}$$

The resulting conductivity reads

$$\bar{\bar{\sigma}}^A = \epsilon_0\omega \begin{bmatrix} i+\Im(S) & -i\Im(D) & 0 \\ i\Im(D) & i+\Im(S) & 0 \\ 0 & 0 & i+\Im(P) \end{bmatrix}. \tag{29}$$

The power absorption can be written as:

$$Q_a^A = \sigma_{l,m}^{A,R}\left(E_l^R E_m^R + E_m^I E_l^I\right) + \sigma_{l,m}^{A,I}\left(E_m^R E_l^I - E_m^I E_l^R\right) \tag{30}$$

where l, m are the indices in tensor notation and R, I represent the real and imaginary parts of the tensor. On the one hand, in this equation the term arising from the imaginary part of $\bar{\bar{\sigma}}^A$ produces no absorption for the diagonal terms, and absorption proportional to the product of fields with radial and azimuthal components. On the other hand, the contribution of the real part $\bar{\bar{\sigma}}^A$, is zero for off-diagonal elements as the real part of the $\bar{\bar{\sigma}}^A$ is null there. Therefore, only the terms proportional to the fields norm squared contribute to power absorption from this part. If we assume that the magnetic field is aligned with the z component, this results in an absorption that follows that

$$Q_a^A \approx \Im(S)\left(|\hat{\boldsymbol{E}}_r|^2 + |\hat{\boldsymbol{E}}_\theta|^2\right) + \Im(P)|\hat{\boldsymbol{E}}_z|^2 + 2\Im(D)(E_r^R E_\theta^I - E_r^I E_\theta^R). \tag{31}$$

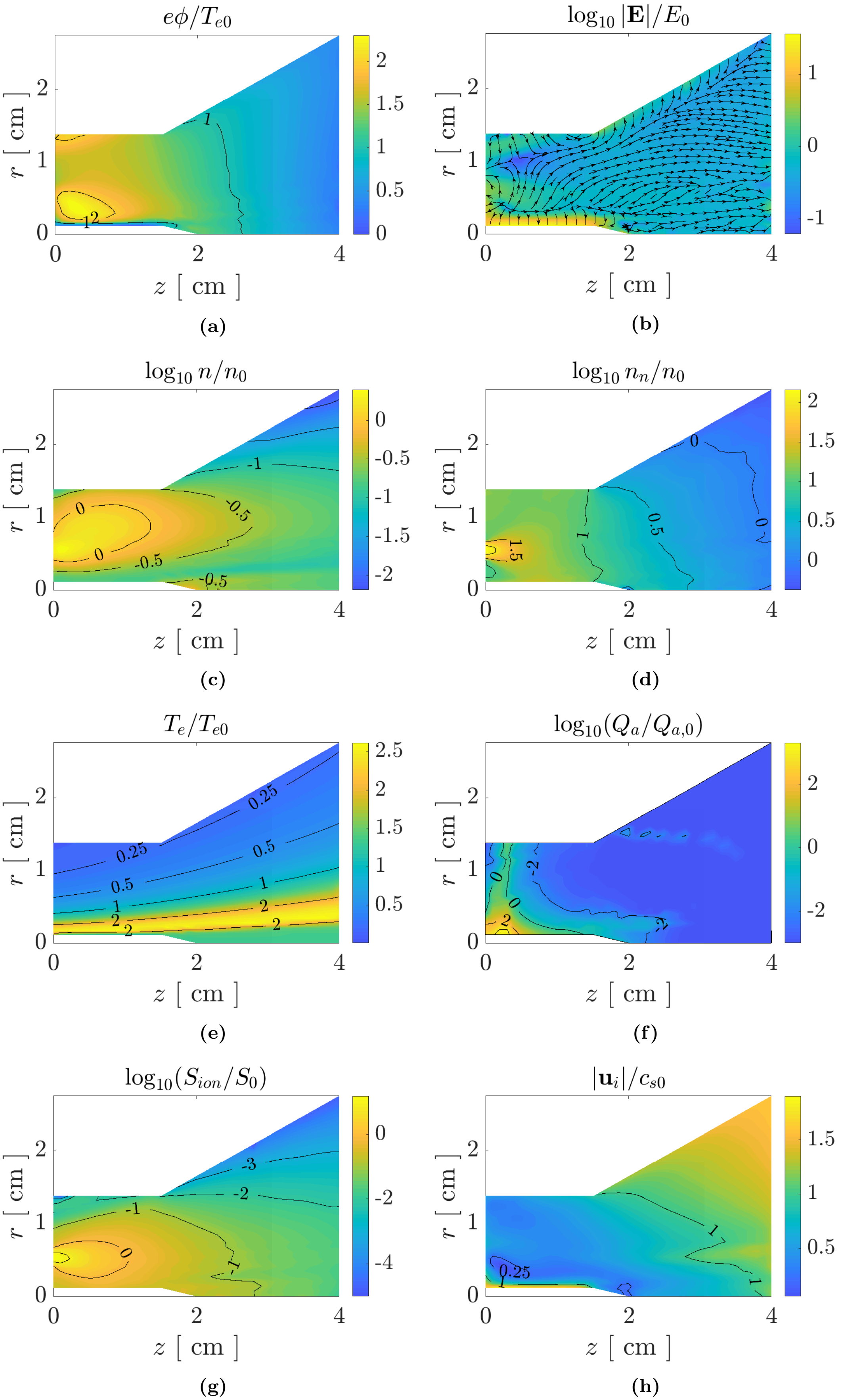

$e\phi/T_{e0}$ (a)

$\log_{10}|\mathbf{E}|/E_0$ (b)

$\log_{10} n/n_0$ (c)

$\log_{10} n_n/n_0$ (d)

T_e/T_{e0} (e)

$\log_{10}(Q_a/Q_{a,0})$ (f)

$\log_{10}(S_{ion}/S_0)$ (g)

$|\mathbf{u}_i|/c_{s0}$ (h)

Figure 5: Results of the transport module (I).

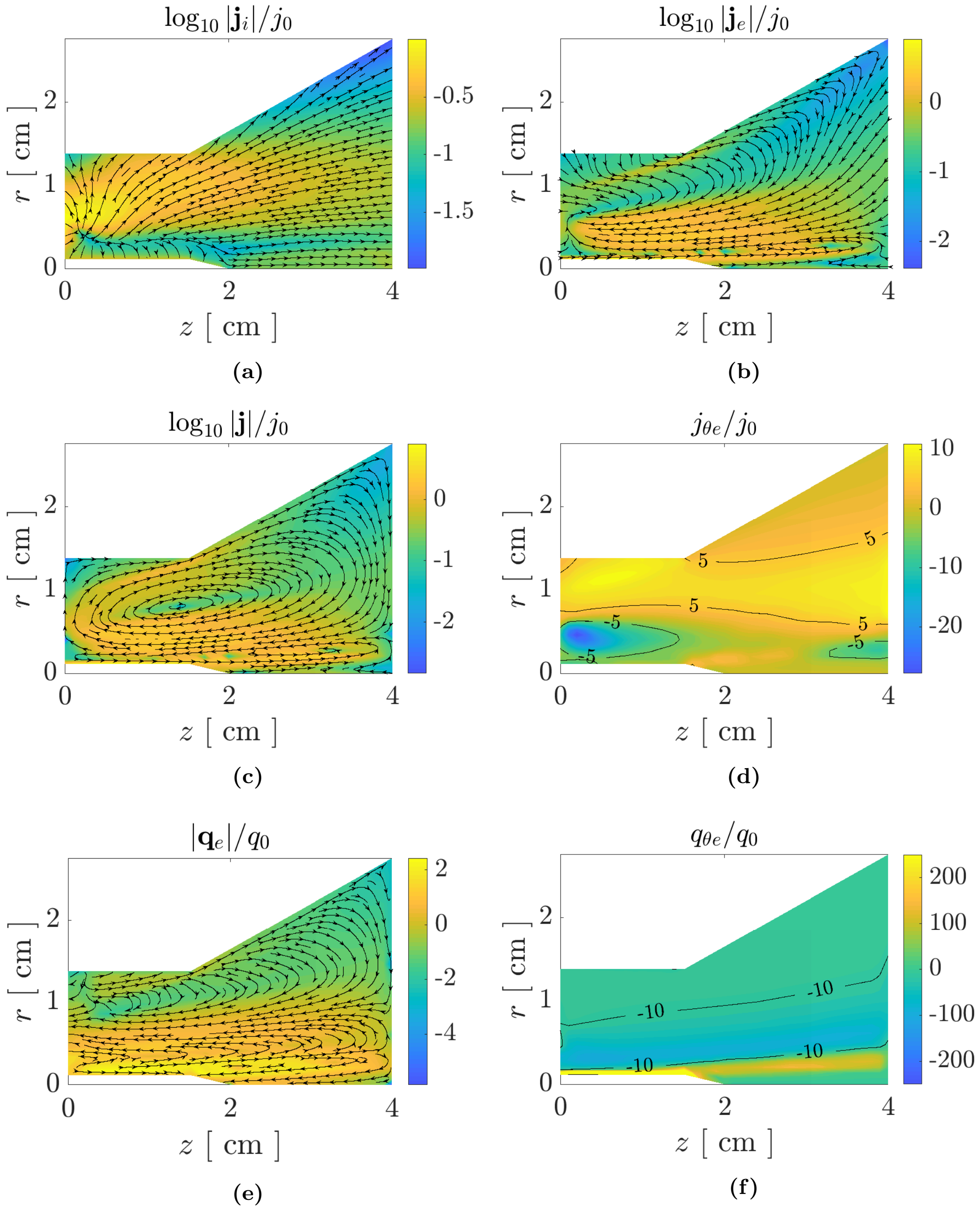

(a) (b) (c) (d) (e) (f)

Figure 6: Results of the transport module (II) and CMA region.

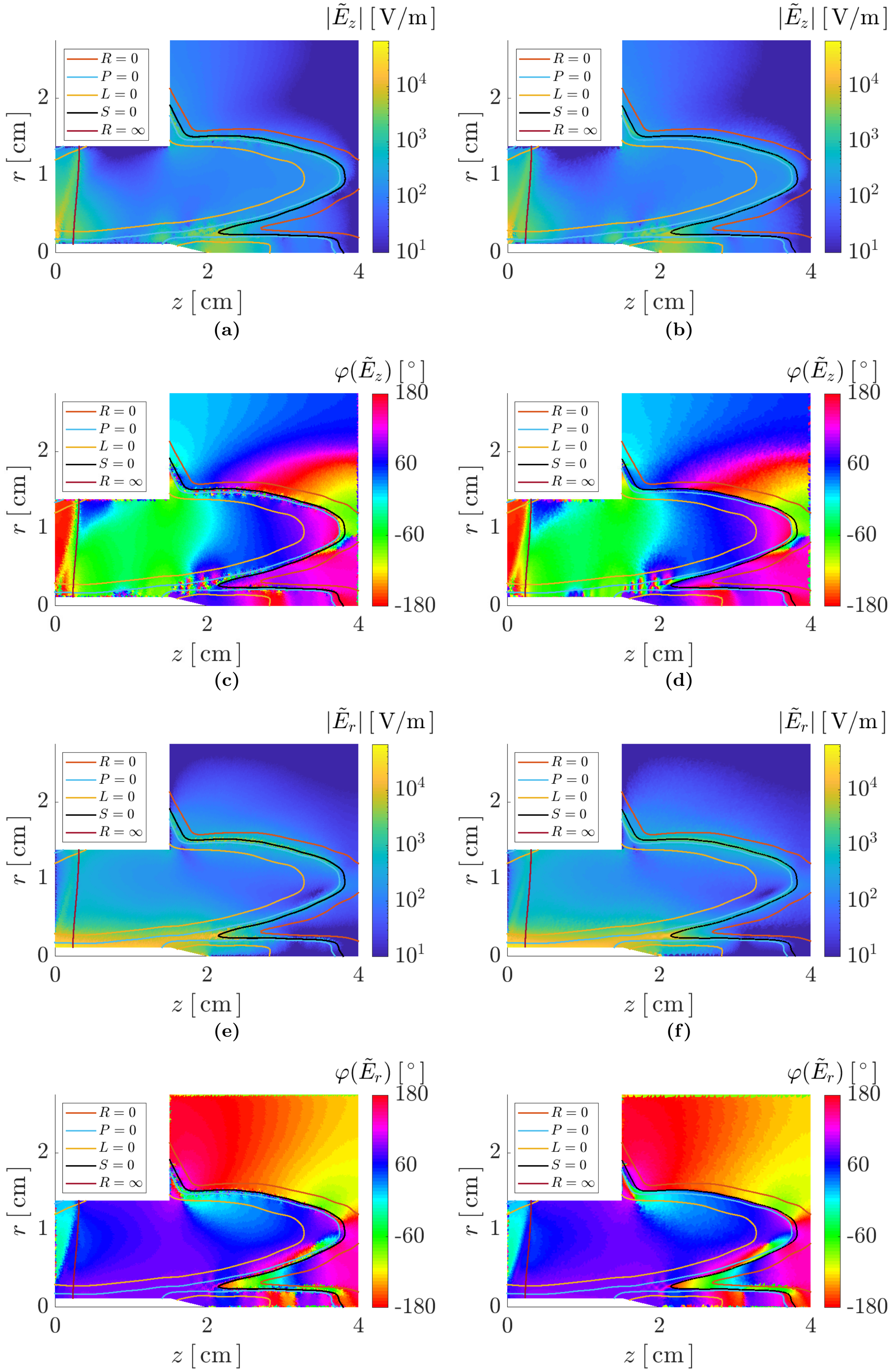

(a) (b) (c) (d) (e) (f) (g) (h)

Figure 8: Wave module results with uniform mesh (left) and predictive refinement (right).

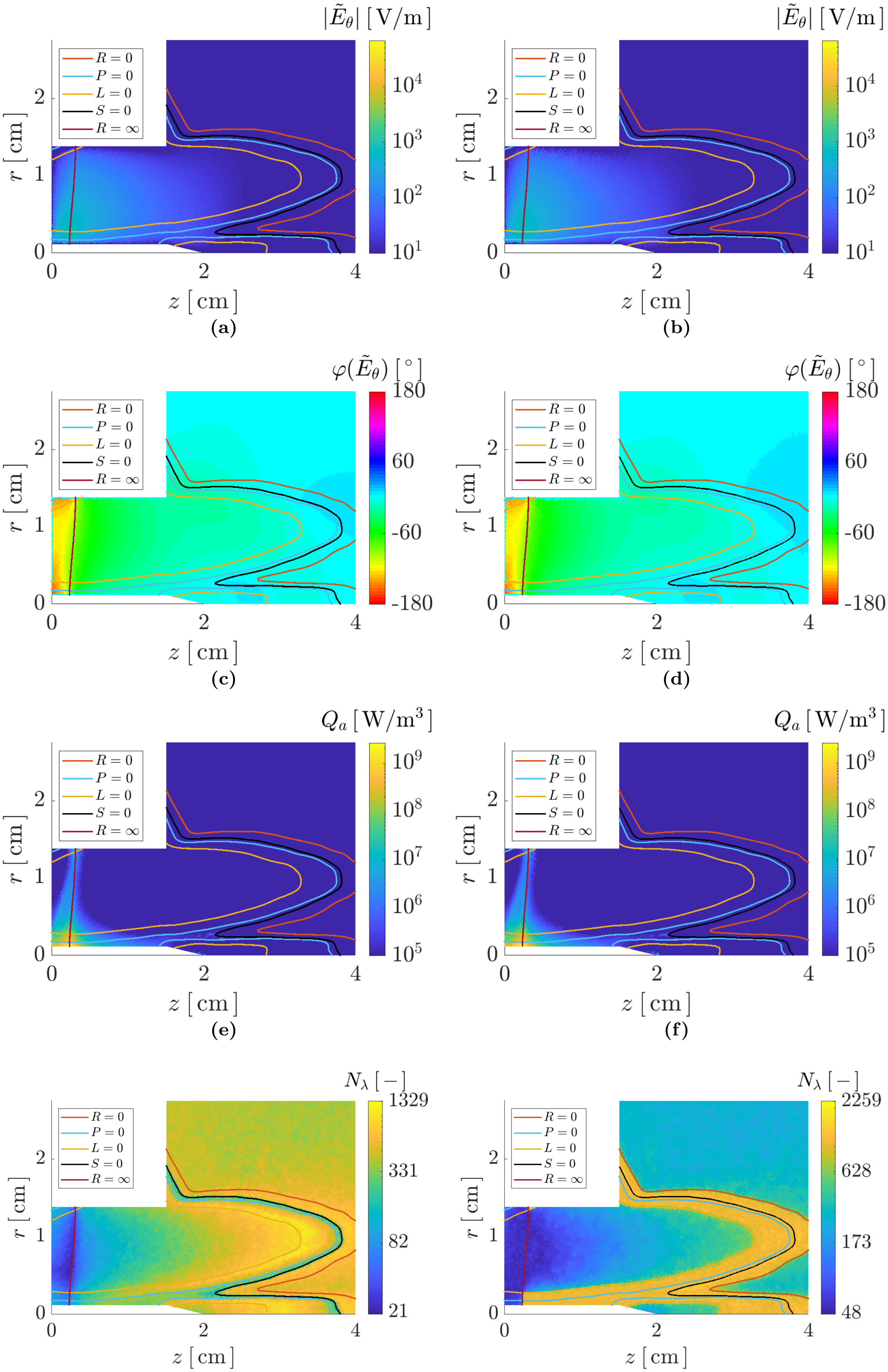

(a) (b)

(c) (d)

(e) (f)

(g) (h)

Figure 9: Wave module results with uniform mesh (left) and predictive refinement (right).

At the ECR resonance, the imaginary part of S reaches its maximum as can be seen in Fig.10a. The imaginary part of P is two orders of magnitude smaller than that of S. The power absorbed is then obtained by both radial and azimuthal fields. As a result of the azimuthal component of the fields being negligible with respect to the radial component, the radial fields dominate the absorption.

Thus, the major contribution to power absorption in a domain dominated dominated by radial fields with a mainly axial magnetic field being aligned with z, is the term $\sigma_R^A|E_r|^2$. This quantity is shown in Figure 10.

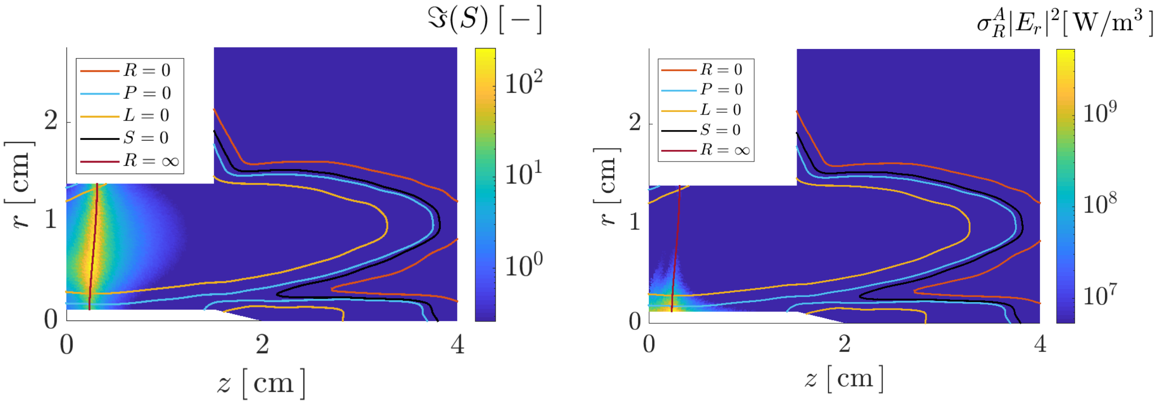

(a)

(b)

Figure 10: Imaginary part of S. Absorbed power contribution.

D. The effect of adaptive refinement to deal with numerical instability associated to an UHR region

Figs. 8 and 9 show a comparison between the self-consistent simulations for a uniform mesh (on the left) with the solutions obtained with a refined mesh. A standard criteria is to define minimum number of cells per wavelength (N_λ), typically of the order of 10. Here we select a minimum of 20 for all the simulations to the highly nonuniform character of the plasma properties and thus the minimum wavelength. The minimum wavelength is computed from the different dispersion relations of each propagating mode given by the collisional cold-plasma model[52,54] taking the properties at every mesh node. For the uniform case, Fig. 9g represents the minimum wavelength divided by the characteristic mesh-cell length which is uniform. The most restrictive regions are in order of importance the vicinity of the ECR and then the upper-hybrid resonance (UHR) region.

As can be seen from results of figures 8c and 8g, a region of high frequency oscillations in the phase is found. The refinement applied to this uniform mesh is depicted by Fig.9h, and it is a result of multiple refinement strategies. The refined mesh is created so that the minimum number of refuses the minimum wavelength to refine the mesh combined with a local refinenement focused on regions 2 3 and 4 of the CMA diagram. This oscillations are found to be of the size of the element. Such noise has been found to have a direct correlation with the location of the upper hybrid resonance region, which is represented in the cold-plasma model by the line S = 0 of the CMA diagram (black solid line). In Ref. 55 it is reported that spurious solutions appear as a numerical instability arising from the use of double-curl formulation of Maxwell's equations near resonances of type S=0. Such resonances are both the so-called lower-hybrid resonance (LHR) and the upper-hybrid resonance (UHR). In the work cited the authors refer to the spurious noise near the LHR. There, the authors present simulations using ERMES,[56] that obtain spurious free solutions through a regularization of the double curl formulation.[57] Although the spurious lower hybrid resonance is not of special interest for ECR thrusters, another resonance of type S=0 arises when the upper-hybrid frequency matches the excitation frequency. This region corresponds to a thin layer located at the black line in Figs.8c and 8d.

The work presented here suggests the existence of this numerical issue for the other case of resonances of type S=0, the upper hybrid resonance. In particular, at the vicinity of such resonances, Eq.(12) reduces to

$$\nabla \times \nabla \times \tilde{E} \approx 0 \tag{32}$$

which has infinitely many solutions of the type $\hat{E} = \nabla\phi$, where ϕ is a scalar potential.

A indicator suggesting that such high frequency noise has spurious character is the fact that the noise has an oscillatory scale of the order of the mesh-cell characteristic length. We can notice this effect comparing Fig.8a and 8b. Simulation results of Fig.8b are a result of the application of local non-uniform refinement based on a target element size. This element size is chosen as a combination of multiple effects. Firstly, the minimum wavelength estimated by the cold-plasma model is calculated for the entire domain, using the plasma properties obtained by the transport module. Secondly, the step in characteristic wavelength in the transition coaxial to thruster chamber is smoothened. Finally, a local refinement is applied to the target increased refinement in regions affected by noise as seen in Figs.8c and 8d. These regions correspond to CMA regions 4 3 and 2 as shown in Fig.7. Note that the noise affects the solution until the L mode cutoff. Afterwards there is region 5 where all waves are evancescent.

However, this refinement, also related to region 3 of the CMA, reduces the propagation of this spurious noise from the region affected to the rest of the domain. This can be seen comparing in Figs.8c and 8g with the adaptive mesh results shown in Figs.8d and 8h. As for the power absorption, the maps are barely affected (see Figs.9e and 9f). As a consequence, the addition of the adaptive refinement to the iterative loop has been disregarded.

V. Concluding remarks and future work

In this paper we present axisymmetric self-consistent solutions of the plasma properties and electromagnetic fields inside an electron-cyclotron resonance thruster. This paper shows the first results of a self-consistent simulation of the axisymmetric RF-generated plasma of an ECR thruster, with the characteristics of the prototype developed at ONERA.

The results show that the solutions of the electromagnetic fields in the thruster are strongly affected by the characteristics of the plasma transport inside the thruster chamber and viceversa.

The main contribution to electromagnetic power absorption is found to be generated by radial electric fields located at the ECR region. As a consequence of combination of perpendicular transport and the close location of the highest power absorption being focused close to the antenna might lead to the considerable power losses to the walls are exhibited.

The simulation shows that the ECRT plasma discharge contains multiple electromagnetic wave propagation regimes, including the presence of a upper-hybrid resonance region (UHR). The topology of the different regions is sensitive to variations of the plasma density profile, which may open or close propagation channels through which the wave power may flow. In other words, the electromagnetic results show good agreement with the different cutoffs and resonances estimated by the CMA diagram of the cold-plasma model.

Numerical treatment of UHR regions presents several difficulties, that will be addressed in future work. A predictive local refinement strategy applied on the meshing of the wave mesh shows substantial mitigation of such numerical difficulties, but does not solve all potential problems.

The addition of the electromagnetic wave module to perform complete, self-consistent simulations to the SURFET code enables the study of the physics of ECR plasma thrusters to improve our understanding of the operation of the device and the dominant physical mechanisms that drive its performance. Due to the high sensitivity experienced in the simulations to the problem parameters, parametric studies and sensitivity analyses different mass flow rates, input power, resonance location, frequency, etc., will be performed to guide thruster design and optimization tasks. Furthermore, a detailed electromagnetic power analysis will be completed. As for the development of the EM-wave module, we will implement all azimuthal wave-modes together the inclusion of more boundary conditions as a general port or a perfectly-matched layer for domain truncation.

Acknowledgments

The authors thank Dr. Rubén Otín for the valuable and insightful discussions. Furthermore the authors thank Sc. D. Syun'ichi Shiraiwa, Dr. Luis Emilio García Castillo and Dr. Adrián Amor for their useful suggestions in the development of the FE EM-wave module. Also mention has to be made to Adrían Domínguez-Vázquez who assisted the authors during the development of the self-consistent simulations in the details related to the PIC module. The research leading to these results has been funded by the European

Union H2020 program under grant agreement 730028 (Project MINOTOR). Additionally, this research has received funding from Spain's Ministry of Science, Innovation and Universities FPU scholarship program with grant FPU17/06352.

References

[1] Miller, D. B., Gloersen, P., Gibbons, E. F., and BenDaniel, D. J., "Cyclotron resonance propulsion system," Tech. rep., General Electric Co. Missile and Space Vehicle Dept., Philadelphia, 1963.

[2] Miller, D. and Gibbons, E., "Experiments with an electron cyclotron resonance plasma accelerator," *AIAA Journal*, Vol. 2, No. 1, 1964, pp. 35–41.

[3] Bethke, G. and Miller, D., "Cyclotron resonance thruster design techniques." *AIAA Journal*, Vol. 4, No. 5, 1966, pp. 835–840.

[4] Crimi, G., Eckert, A., and Miller, D., "Microwave Driven Magnetic Plasma Accelerator Studies (Cyclops)," 1967.

[5] Sercel, J., "Electron-cyclotron-resonance (ECR) plasma acceleration," *AIAA 19th Fluid Dynamics, Plasma Dynamics and Lasers Conference*, 1987.

[6] SERCEL, J., "Electron-cyclotron-resonance (ECR) plasma thruster research," *24th Joint Propulsion Conference*, 1988, p. 2916.

[7] Sercel, J., *An experimental and theoretical study of the ECR plasma engine*, Ph.D. thesis, California Institute of Technology, 1993.

[8] MILLER, D., GIBBONS, E., and GLOERSEN, P., "Cyclotron resonance propulsion system," *Electric Propulsion Conference*, 1962, p. 2.

[9] Sercel, J., "Simple model of plasma acceleration in a magnetic nozzle," *21st International Electric Propulsion Conference*, Vol. 1, 1990.

[10] Geller, R., "ECRIS: The electron cyclotron resonance ion sources," *Annual Review of Nuclear and Particle Science*, Vol. 40, No. 1, 1990, pp. 15–44.

[11] Kuninaka, H., Nishiyama, K., Funaki, I., Yamada, T., Shimizu, Y., and Kawaguchi, J., "Powered flight of electron cyclotron resonance ion engines on Hayabusa explorer," *Journal of Propulsion and Power*, Vol. 23, No. 3, 2007, pp. 544–551.

[12] Packan, D., Elias, P.-Q., Jarrige, J., Merino, M., Sánchez-Villar, A., Ahedo, E., Peyresoubes, G., Holste, K., Klar, P., Bekemans, M., Scalais, T., Bourguignon, E., Zurbach, S., Mares, M., Hooque, A., and Favier, P., "The MINOTOR H2020 project for ECR thruster development," 35^{th} *International Electric Propulsion Conference*, No. IEPC-2017-547, Electric Rocket Propulsion Society, 2017.

[13] Jarrige, J., Elias, P.-Q., Cannat, F., and Packan, D., "Characterization of a coaxial ECR plasma thruster," *44th AIAA Plasmadynamics and Lasers Conference, San Diego*, 2013.

[14] Domínguez-Vázquez, A., *Axisymmetric simulaton codes for Hall effect thrusters and plasma plumes*, Ph.D. thesis, Universidad Carlos III de Madrid, Leganés, Spain, To be defended, 2019.

[15] Domínguez-Vázquez, A., Fajardo, P., and Ahedo, E., "Analysis of the plasma discharge in a Hall thruster via a hybrid 2D code," 36^{th} *International Electric Propulsion Conference*, No. IEPC-2019-579, Electric Rocket Propulsion Society, Vienna, Austria, 2019.

[16] Pérez-Grande, D., *Fluid modeling and simulation of the electron population in Hall effect thrusters with complex magnetic topologies*, Ph.D. thesis, Universidad Carlos III de Madrid, Leganés, Spain, 2018.

[17] Pérez-Grande, D., Zhou, J., Domínguez-Vázquez, A., Fajardo, P., and Ahedo, E., "Development updates for a two-dimensional axisymmetric hybrid code for plasma thruster discharges," 35^{th} *International Electric Propulsion Conference*, No. IEPC-2017-201, Electric Rocket Propulsion Society, Atlanta, GA, 2017.

[18] Sánchez-Villar, A. and Merino, M., "Advances in Wave-Plasma Modelling in ECR Thrusters," *Space Propulsion Conference 2018*, No. 00346, Association Aéronautique et Astronautique de France, Seville, Spain, 2018.

[19] Greenwood, A. D. and Jin, J.-M., "A novel efficient algorithm for scattering from a complex BOR using mixed finite elements and cylindrical PML," *IEEE transactions on antennas and propagation*, Vol. 47, No. 4, 1999, pp. 620–629.

[20] Greenwood, A. D. and Jin, J.-M., "Finite-element analysis of complex axisymmetric radiating structures," *IEEE Transactions on Antennas and Propagation*, Vol. 47, No. 8, 1999, pp. 1260–1266.

[21] Bertelli, N., Jaeger, E., Hosea, J., Phillips, C., Berry, L., Gerhardt, S., Green, D., LeBlanc, B., Perkins, R., Ryan, P. M., et al., "Full wave simulations of fast wave heating losses in the scrape-off layer of NSTX and NSTX-U," *Nuclear Fusion*, Vol. 54, No. 8, 2014, pp. 083004.

[22] Kim, E.-H., Bertelli, N., Johnson, J., Valeo, E., and Hosea, J., "2D full-wave simulation of waves in space and tokamak plasmas," *EPJ Web of Conferences*, Vol. 157, EDP Sciences, 2017, p. 02005.

[23] Gammino, S., Ciavola, G., Celona, L. G., Mascali, D., and Maimone, F., "Numerical simulations of the ECR heating with waves of different frequency in electron cyclotron resonance ion sources," *IEEE Transactions on Plasma Science*, Vol. 36, No. 4, 2008, pp. 1552–1568.

[24] Asmussen, J., Grotjohn, T. A., Mak, P., and Perrin, M. A., "The design and application of electron cyclotron resonance discharges," *IEEE transactions on plasma science*, Vol. 25, No. 6, 1997, pp. 1196–1221.

[25] Brambilla, M., "Self-consistent field and power absorption from electron cyclotron resonance in a high frequency plasma accelerator," *Plasma Physics*, Vol. 10, No. 4, 1968, pp. 359.

[26] Jaeger, F., Lichtenberg, A., and Lieberman, M., "Theory of electron cyclotron resonance heating. I. Short time and adiabatic effects," *Plasma Physics*, Vol. 14, No. 12, 1972, pp. 1073.

[27] Lieberman, M. and Lichtenberg, A., "Theory of electron cyclotron resonance heating. II. Long time and stochastic effects," *Plasma Physics*, Vol. 15, No. 2, 1973, pp. 125.

[28] Williams, J. and Wilbur, P., "Electron emission from a hollow cathode-based plasma contactor," *J. Spacecr. Rockets*, Vol. 29, 1992, pp. 820–829.

[29] Cluggish, B. P. and Kim, J.-S., "Modeling of wave propagation and absorption in electron cyclotron resonance ion source plasmas," *Nuclear Instruments and Methods in Physics Research Section A: Accelerators, Spectrometers, Detectors and Associated Equipment*, Vol. 664, No. 1, 2012, pp. 84–97.

[30] Manheimer, W. M., "A Simple Scheme for Implementing Wave Absorption in Quasi-Neutral PIC Simulations of ECR Plasma," Tech. rep., NAVAL RESEARCH LAB WASHINGTON DC FUNDAMENTAL PLASMA PROCESSES, 1998.

[31] Cardinali, A., Melazzi, D., Manente, M., and Pavarin, D., "Ray-tracing WKB analysis of Whistler waves in non-uniform magnetic fields applied to space thrusters," *Plasma Sources Science and Technology*, Vol. 23, No. 1, 2014, pp. 015013.

[32] Muta, H., Sakoda, T., Ueda, Y., and Kawai, Y., "One-dimensional simulation of microwave propagation in electron cyclotron resonance plasmas," *Japanese journal of applied physics*, Vol. 36, No. 2R, 1997, pp. 872.

[33] Muta, H., Ueda, Y., and Kawai, Y., "Three-dimensional simulation of microwave propagation in an electron cyclotron resonance plasma," *Japanese journal of applied physics*, Vol. 36, No. 7S, 1997, pp. 4773.

[34] Yasaka, Y., Fukuyama, A., Hatta, A., and Itatani, R., "Two-dimensional modeling of electron cyclotron resonance plasma production," *Journal of applied physics*, Vol. 72, No. 7, 1992, pp. 2652–2658.

[35] Yasaka, Y. and Uda, N., "Practical scheme for three-dimensional simulation of electron cyclotron resonance plasma reactors," *Journal of Applied Physics*, Vol. 89, No. 7, 2001, pp. 3594–3601.

[36] Zhou, J., , Merino, M., and Ahedo, E., "Numerical Simulations of the Plasma Discharge in a Helicon Plasma Thruster," 36th *International Electric Propulsion Conference*, No. IEPC-2019-330, Electric Rocket Propulsion Society, Vienna, Austria, 2019.

[37] Zhou, J., Pérez-Grande, D., Fajardo, P., and Ahedo, E., "Numerical treatment of a magnetized electron fluid within an electromagnetic plasma thruster code," *Submitted to PSST*, 2019.

[38] Domínguez-Vázquez, A., Cichocki, F., Merino, M., Fajardo, P., and Ahedo, E., "2D and 3D Hybrid PIC/Fluid Modelling of Electric Thruster Plumes," 35th *International Electric Propulsion Conference*, No. IEPC-2017-209, Electric Rocket Propulsion Society, Atlanta, GA, 2017.

[39] Domínguez-Vázquez, A., Taccogna, F., and Ahedo, E., "Particle modeling of radial electron dynamics in a controlled discharge of a Hall thruster," *Plasma Sources Science and Technology*, Vol. 27, No. 6, 2018, pp. 064006.

[40] Domínguez-Vázquez, A., Cichocki, F., Merino, M., Fajardo, P., and Ahedo, E., "Axisymmetric plasma plume characterization with 2D and 3D particle codes," *Plasma Sources Science and Technology*, Vol. 27, No. 10, 2018, pp. 104009.

[41] Zhou, J., Domínguez-Vázquez, A., Pérez-Grande, D., Fajardo, P., and Ahedo, E., "An axisymmetric hybrid model for the plasma transport in a helicon plasma thruster," *Space Propulsion Conference 2018*, No. 00308, Association Aéronautique et Astronautique de France, Seville, Spain, 2018.

[42] Ahedo, E. and Pablo, V. d., "Combined effects of electron partial thermalization and secondary emission in Hall thruster discharges," *Physics of Plasmas*, Vol. 14, 2007, pp. 083501.

[43] "MFEM: Modular Finite Element Methods Library," http://mfem.org.

[44] Merino, M., Sánchez-Villar, A., Ahedo, E., Bonoli, P., Lee, J., Ram, A., and Wright, J., "Wave Propagation and Absorption in ECR Plasma Thrusters," 35th *International Electric Propulsion Conference*, No. IEPC-2017-105, Electric Rocket Propulsion Society, Atlanta, GA, 2017.

[45] Geuzaine, C. and Remacle, J.-F., "Gmsh: A 3-D finite element mesh generator with built-in pre-and post-processing facilities," *International journal for numerical methods in engineering*, Vol. 79, No. 11, 2009, pp. 1309–1331.

[46] Yee, K., "Numerical solution of initial boundary value problems involving Maxwell's equations in isotropic media," *IEEE Transactions on antennas and propagation*, Vol. 14, No. 3, 1966, pp. 302–307.

[47] Jiang, B.-N., Wu, J., and Povinelli, L. A., "The origin of spurious solutions in computational electromagnetics," *Journal of computational physics*, Vol. 125, No. 1, 1996, pp. 104–123.

[48] Hara, M., Wada, T., Fukasawa, T., and Kikuchi, F., "A three dimensional analysis of RF electromagnetic fields by the finite element method," *IEEE Transactions on Magnetics*, Vol. 19, No. 6, 1983, pp. 2417–2420.

[49] Monk, P., *Finite element methods for Maxwell's equations*, Oxford University Press, 2003.

[50] Jin, J.-M. and Riley, D. J., *Finite element analysis of antennas and arrays*, John Wiley & Sons, 2009.

[51] Nédélec, J.-C., "Mixed finite elements in $\mathbb{R}^3$," *Numerische Mathematik*, Vol. 35, No. 3, 1980, pp. 315–341.

[52] Stix, T. H., *Waves in plasmas*, Springer Science & Business Media, 1992.

[53] Brambilla, M., *Kinetic theory of plasma waves: homogeneous plasmas*, No. 96, Oxford University Press, 1998.

[54] Heald, M. A. and Wharton, C. B., *Plasma diagnostics with microwaves*, Wiley, 1965.

[55] Otin, R., Tierens, W., Parra, F., Aria, S., Lerche, E., Jacquet, P., Monakhov, I., Dumortie, P., Van Compernolle, B., and Contributors, J., "Full Wave Simulation of RF Waves in Cold Plasma with the Stabilized Open-Source Finite Element Tool ERMES," .

[56] Otin, R., "ERMES: A nodal-based finite element code for electromagnetic simulations in frequency domain," *Computer Physics Communications*, Vol. 184, No. 11, 2013, pp. 2588–2595.

[57] Hazard, C. and Lenoir, M., "On the solution of time-harmonic scattering problems for Maxwell's equations," *SIAM Journal on Mathematical Analysis*, Vol. 27, No. 6, 1996, pp. 1597–1630.